Electron dynamics in radio frequency magnetron sputtering argon discharges with a dielectric target

Bocong Zheng[1,5], **Yangyang Fu**[2,3,5], **Keliang Wang**[1],
Thomas Schuelke[1,3] **and Qi Hua Fan**[1,3,4,*]

[1] Fraunhofer Center for Coatings and Diamond Technologies, Michigan State University, East Lansing, MI 48824, United States of America
[2] Department of Computational Mathematics, Science and Engineering, Michigan State University, East Lansing, MI 48824, United States of America
[3] Department of Electrical and Computer Engineering, Michigan State University, East Lansing, MI 48824, United States of America
[4] Department of Chemical Engineering and Materials Science, Michigan State University, East Lansing, MI 48824, United States of America

E-mail: bzheng@fraunhofer.org, fuyangya@msu.edu and qfan@egr.msu.edu

CrossMark

Abstract

We demonstrate a self-consistent and complete description of electron dynamics in a typical electropositive radio frequency magnetron sputtering (RFMS) argon discharge with a dielectric target. The electron dynamics, including the electron power absorption dynamics in one radio frequency (RF) period, is studied via a fully kinetic 2d3v particle-in-cell/Monte Carlo collision (PIC/MCC) electrostatic simulation. The interplay between the fundamental plasma parameters is analyzed through their spatiotemporal dynamics. Due to the influence of magnetic trap on the electron transport, a spatially dependent charging that perturbs the electric potential is observed on the dielectric target surface, resulting in a spatially dependent ion energy distribution along the target surface. The $E \times B$ drift-to-discharge current ratio is in approximate agreement with Bohm diffusion. The electron power absorption can be primarily decoupled into the positive Ohmic power absorption in the bulk plasma region and the negative pressure-induced power absorption near the target surface. Ohmic power absorption is the dominant electron power absorption mechanism, mostly contributed by the azimuthal electron current. The power absorption due to electron inertial effects is negligible on time-average. Both the maximum power absorption and dissipation of electrons appear in the bulk plasma region during the second half of the RF period, implying a strong electron trapping in magnetron discharges. The contribution of secondary electrons is negligible under typical RFMS discharge conditions.

Keywords: radio frequency magnetron sputtering, electron dynamics, particle-in-cell, magnetized plasma, capacitively coupled plasmas, electron power absorption, moments of Boltzmann equation

S Supplementary material for this article is available online

(Some figures may appear in colour only in the online journal)

---

*Author to whom any correspondence should be addressed.
[5]These two authors contributed equally to this work.

1. Introduction

Capacitively coupled radio frequency (RF) plasmas are widely used in material processing [1, 2]. Among RF plasmas, radio frequency magnetron sputtering (RFMS) discharge is one of the most commonly used plasma sources, and has many unique advantages comparing with direct current magnetron sputtering (DCMS) discharges [3, 4]. In RFMS discharges, the target can be selected from a wide variety of materials, including semiconductors and insulators. The magnetron can maintain a stable discharge and suppress the formation of micro-arcs because the charges accumulated on an insulating target surface can be neutralized within one RF period. Due to the above advantages, RFMS is widely used for fabricating high-quality thin films of various functions, such as transparent conducting films [5–12], photocatalytic thin films [13], piezoelectric thin films [14], solar cells [15], ferroelectric thin films [16–18], nanostructural thin films [19, 20], electroceramic thin films [21], high-entropy alloy films [22], biocompatible thin films [23, 24], and colossal magnetoresistance thin films [25]. In physical vapor deposition processes, the properties of deposited thin films depend on the characteristics of the deposition flux [26], such as the ion energy distribution [27–30] and the ion-to-neutral flux ratio [31] of deposited species at the substrate, which are directly determined by the electron dynamics. This is because the electrons are responsible for the generation of ions via ionization collisions. The generated ions are accelerated by the time-averaged electric field toward the target surface, where they remove target material through sputtering and generate the deposition flux. Therefore, a fundamental knowledge and a thorough understanding of the electron dynamics in RFMS discharges are of essential significance for controlling and optimizing the discharge processes as well as the properties of deposited thin films.

In contrast to the wide applications of RFMS discharge, its electron dynamics is still a topic rather poorly understood. Previous studies on the RFMS discharge, including experimental diagnoses [27–38] and theoretical analyses [39, 40], have obtained the primary plasma parameters, such as the plasma density, the electron temperature, the ion and electron energy distributions, as well as their spatial and temporal variations. However, due to the complexity of magnetron discharges, accurate diagnoses and theoretical studies on electron dynamics under actual geometry and magnetic field distribution are less investigated.

In addition to experimental diagnosis and theoretical analysis, plasma modeling is also an essential tool in the investigation of magnetron discharges. A simple but commonly used plasma model is the zero-dimensional global model, which has been adopted to study various characteristics of magnetron discharges [41–54], such as electron heating [43, 46], gas rarefaction [42], self-sputtering [44, 49], target poisoning [48, 50], etc. Albeit the above-mentioned studies are mainly for DCMS, the global model has also been applied in investigating the RFMS discharge [55]. The global model is not computationally expensive. It provides space-averaged plasma

parameters and their relationships with process parameters, which helps guide the application of magnetron discharges. Other commonly used models include the fluid model [56–58] and the Monte Carlo model [59]. However, these models are self-inconsistent and incomplete; they cannot provide a detailed understanding of the rather complicated RFMS discharge.

Particle-in-cell/Monte Carlo collision (PIC/MCC) simulation overcomes the above-mentioned disadvantages, and provides a complete and self-consistent picture of magnetron discharges [60]. The main disadvantage is the long computation time. PIC simulations have been performed in investigating RFMS discharges for more than two decades [61–70]. The fundamental plasma parameters and their temporal and spatial distributions have been successfully simulated and are consistent with experimental results. However, little is known about the electron dynamics of RFMS discharge in a RF period, especially the electron power absorption dynamics.

In low-temperature plasmas, ions and reactive radicals are generated primarily through collisional reactions between energetic electrons and other species. For example, to ionize the background gas, electrons must have a certain energy, i.e., the ionization threshold energy of the gas species. Therefore, one of the most fundamental questions in RFMS, as in other low-temperature RF discharges, is the electron power absorption mechanism, i.e., how the energy is transferred from the electric field to the electrons and then redistributed among them. Electron power absorption has also been historically referred to as 'electron heating', although in fact the two are not the same, since the power absorption resulting from electron acceleration in one direction does not necessarily imply an increase in electron temperature, which requires subsequent isotropization [71]. However, for simplicity, the historical terminology 'heating' or 'cooling' is occasionally used to describe an increase or decrease in the spatiotemporal electron power absorption at a certain moment and location. A considerable amount of work has been reported on the electron power absorption in unmagnetized [72–95] and magnetized [56, 58, 96–107] capacitively coupled RF discharges. Through the above investigation, two of the most important electron power absorption mechanisms are identified, i.e., the collisional or Ohmic power absorption due to electron-neutral collisions, and the collisionless or stochastic heating due to momentum transfer from the oscillating sheath. Stochastic electron power absorption is generally considered as the dominant power absorption mechanism in low-pressure RF discharges. On the other hand, the dominant power absorption mechanism changes from a stochastic to a bulk Ohmic power absorption under a low pressure (e.g., 10 mTorr) if a small transverse magnetic field of 10 G is introduced [96, 108]. This enhanced Ohmic power absorption is attributed to the azimuthal electron current, i.e., the $\boldsymbol{E} \times \boldsymbol{B}$ drift current of electrons [40, 106]. However, this conclusion has not been verified for RFMS discharges in a self-consistent manner and the details are unclear.

In this work, we investigate the electron dynamics in RFMS discharges operated in argon at a frequency of 13.56 MHz, a

driving voltage of 200 V, and a gas pressure of 10 mTorr via a fully kinetic PIC/MCC simulation. The spatial and temporal dynamics of the fundamental plasma parameters, such as electron densities, electric potentials and fields, as well as electron current densities during one RF period are investigated in detail. Animations are provided in the supplementary materials (https://stacks.iop.org/PSST/30/035019/mmedia) to visually demonstrate the spatiotemporal evolution of these parameters. This paper describes a scenario of electropositive RFMS discharge under typical parameters, including most of the characteristics of electron dynamics under low-pressure magnetized conditions. This paper is structured in the following way: section 2 demonstrates the discharge setup, introduces the theoretical background for investigating the electron power absorption based on a moment analysis of the Boltzmann equation, and describes the PIC/MCC simulation. Section 3 illustrates the electron dynamics during one RF period in four subsections: subsection 3.1 presents the interplay between the electron density and the electric potential and field; subsection 3.2 discusses the phase difference and the amplitude ratio of the electron current density in different directions; subsection 3.3 investigates the different mechanisms of electron power absorption; subsection 3.4 illustrates the ionization rate and discusses the influence of secondary electrons. Finally, conclusions are provided in section 4.

2. Modeling and simulation

2.1. Discharge setup

Figure 1(a) illustrates the schematic of a typical planar RF magnetron sputtering set-up. Plasmas are generated between a dielectric target and the upper chamber wall separated by 3 cm in the $y-$ direction, with a reflection plane at $x = 0$ cm and confined by the left and right chamber walls. The dielectric target is 0.6 cm in thickness and 5.5 cm in width. The backing plate below the dielectric target is connected to a voltage source which supplies an RF voltage of $V(t) = 200 \cdot \sin(2\pi f t)$ [V], where $f = 1/T = 13.56$ MHz is the driving frequency with T being the RF period. Since the discharge is symmetrical to the central reflection plane, half of the chamber is selected as the simulation region and enclosed by red lines. In the selected simulation region, a balanced magnetic field is created by two magnets located under the target, as shown in figure 1(b). Due to the magnetic trap, the magnetron plasma is generally nonuniform and concentrated above the 'racetrack' area, where the magnetic field lines are parallel to the target surface and the plasma density is the highest. For this configuration, the maximum parallel magnetic field B_x over the target surface is about 240 G at $x = 2.9$ cm. Other input parameters can be found in table 1.

The external circuit model with a capacitor is not adopted in this simulation for the following reasons. For most capacitively coupled discharge chambers, the geometry is asymmetric, i.e., the area of the powered electrode is smaller than the area of the grounded electrode. In the presence of an external circuit blocking capacitor or an insulating dielectric on the electrode, electrons are easily collected whenever the electrode becomes
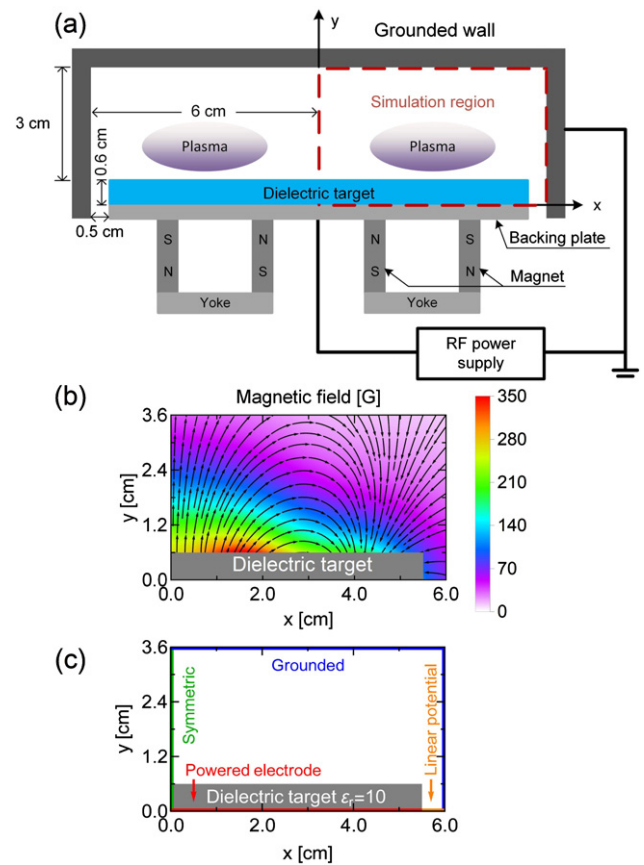
Figure 1. (a) Schematic of a planar RF magnetron sputtering set-up, and the corresponding (b) magnetic field distribution and (c) boundary conditions in the simulation region.

Table 1. The input parameters for the simulation.

Parameter	Value
Gas pressure	10 mTorr
Gas temperature	300 K
Voltage amplitude	200 V
Driving frequency	13.56 MHz
SEE coefficient	0
Electron sticking coefficient	0.5

positive because the mobility of electrons is much higher than that of ions. Therefore, a DC bias is generated at the powered electrode to balance the positive and negative charge fluxes arriving at the electrode. This geometric asymmetry effect has been studied decades ago [109, 110]. For an external circuit model, an insulating layer over the powered electrode instead of using a blocking capacitor is electrically unchanged and an appreciable voltage will still be developed between the bulk plasma and the smaller electrode [111]. Under the geometric conditions studied here, the backing plate is blocked from the plasma by the dielectric target and no net charge can be received; the self-bias is expected to be formed on the dielectric target surface instead of on the backing plate. Therefore, a predefined sinusoidal voltage on the backing plate is adopted in the simulation. Experimentally, in RFMS discharges with a

dielectric target, no DC bias voltage can be measured on the backing plate isolated from the plasma [63].

The boundary conditions for the 2D PIC simulation are illustrated in figure 1(c), as follows:

(a) The left boundary at $x = 0$ cm is symmetric, where particles are reflected and the electric field E_x is 0.

(b) The top and right boundaries at $y = 3.6$ cm and $x = 6$ cm are grounded and the electric potential $\varphi = 0$, particles reaching these boundaries are absorbed.

(c) At the gap at $y = 0$ cm and $x = 5.5$–6 cm, particles are absorbed and the potential varies linearly.

(d) On the backing plate connected to the dielectric target, at $y = 0$ cm and $x = 0$–5.5 cm, a sinusoidal periodic voltage with an amplitude of 200 V is applied.

(e) The region of $0\,\text{cm} \leqslant x \leqslant 5.5\,\text{cm}$ and $0\,\text{cm} \leqslant y \leqslant 0.6\,\text{cm}$ in the simulation region is occupied by the dielectric target with a relative permittivity of 10.

2.2. Theoretical background

Moment analysis of the Boltzmann equation has been successfully applied in investigating the electron dynamics of one-dimensional unmagnetized [71, 88, 94, 112], magnetized [106, 107], electronegative [107, 113], and two-dimensional unmagnetized [114] capacitively coupled discharges. Here, we use this rigorous analysis to study the electron dynamics of the two-dimensional magnetized RFMS discharge in a self-consistent manner. The magnetized Boltzmann equation for electrons is

$$\frac{\partial f_e}{\partial t} + \boldsymbol{v} \cdot \nabla f_e - \frac{e}{m_e}(\boldsymbol{E} + \boldsymbol{v} \times \boldsymbol{B}) \cdot \nabla_v f_e = \left.\frac{\partial f_e}{\partial t}\right|_c, \quad (1)$$

where f_e is the electron distribution function, $\boldsymbol{v}$ the velocity, m_e and e the electron mass and charge, t the time, $\boldsymbol{E}$ and $\boldsymbol{B}$ the electric and magnetic fields. Multiplying the Boltzmann equation by $\boldsymbol{v}$ and integrating all terms of equation (1) over the velocity space, we obtain the momentum conservation equation for electrons

$$m_e n_e \frac{\partial \boldsymbol{u}_e}{\partial t} + m_e(\boldsymbol{\Gamma}_e \cdot \nabla)\boldsymbol{u}_e = -en_e(\boldsymbol{E} + \boldsymbol{u}_e \times \boldsymbol{B}) \\ - \nabla \cdot \overset{\leftrightarrow}{\boldsymbol{\Pi}}_e + \left(\frac{\partial \rho_e}{\partial t}\right)_c, \quad (2)$$

where n_e, $\boldsymbol{u}_e$, $\boldsymbol{\Gamma}_e$, $\overset{\leftrightarrow}{\boldsymbol{\Pi}}_e$ and $(\partial \rho_e/\partial t)_c$ are the electron density, drift velocity, drift flux, pressure tensor and change of momentum due to collisions, respectively [106]. For the two-dimensional simulation shown in figure 1, the electric field is in the x–y plane. Hence, the electron power density can be written as

$$P_e(x, y, t) = \boldsymbol{J}_e \cdot \boldsymbol{E} = J_{ex}E_x + J_{ey}E_y, \quad (3)$$

where $\boldsymbol{J}_e = -en_e\boldsymbol{u}_e$ is the electron current density in the x–y plane. Multiplying each component of equation (2) in different directions with the corresponding drift velocities, we obtain the electron mechanical energy conservation equations in the $x-$, $y-$ and $z-$ directions. The sum of these equations gives the total electron mechanical energy conservation equation,

$$P_e = P_{acc} + P_{in} + P_{press} + P_{Ohmic}, \quad (4)$$

where

$$P_{acc} = m_e n_e \sum_i u_{ei} \frac{\partial u_{ei}}{\partial t},$$

$$P_{in} = m_e \sum_i u_{ei} \left(\Gamma_{ex}\frac{\partial u_{ei}}{\partial x} + \Gamma_{ey}\frac{\partial u_{ei}}{\partial y}\right),$$

$$P_{press} = \sum_i u_{ei}\left(\frac{\partial \Pi_{exi}}{\partial x} + \frac{\partial \Pi_{eyi}}{\partial y}\right), \quad (5)$$

$$P_{Ohmic} = -\sum_i u_{ei}\left(\frac{\partial \rho_{ei}}{\partial t}\right)_c,$$

are the electron power absorption components due to the acceleration term, the inertial term, the pressure-induced effects, and the collisional dynamics. $i = x, y, z$ denotes the axis coordinate. P_{acc} is the power absorption contributed by the acceleration explicitly caused by the time-varying drift velocity $\boldsymbol{u}_e$; therefore, $P_{acc} = 0$ is expected in a steady-state discharge without induction of instability. P_{in} is the power absorption contributed by the inertial term $(\boldsymbol{\Gamma}_e \cdot \nabla)\boldsymbol{u}_e$ and is due to the spatially varying $\boldsymbol{u}_e$; therefore, P_{in} can exist even for steady-state discharges. P_{press} is contributed by the force density obtained from the divergence of the pressure tensor. A non-zero electron pressure tensor divergence $\nabla \cdot \overset{\leftrightarrow}{\boldsymbol{\Pi}}_e$ indicates that there are non-zero gradients in some pressure components in a small volume, i.e., the pressure components vary in some directions. This pressure-induced net force does positive (heating) or negative (cooling) work on the electrons in this volume. While P_{acc}, P_{in}, and P_{press} are generally assigned to collisionless phenomena, P_{Ohmic} contributed by the time rate of momentum transfer per unit volume due to electron collisions with other species. P_{Ohmic} represents the power density required for the electron motion to overcome the collision-induced friction. Since collisions generally impede the motion of electrons, P_{Ohmic} is generally positive. The above moment analysis of the Boltzmann equation provides a consistent and complete description of electron power absorption and clearly shows when and where electrons gain and lose their energy. The contribution of Hall fields are eliminated since $\boldsymbol{u}_e \cdot \boldsymbol{E}_H = 0$, where the Hall field $\boldsymbol{E}_H = (-u_{ez}B_y, u_{ez}B_x, u_{ex}B_y - u_{ey}B_x)$. Note that a negative power absorption in the spatiotemporal profiles is possible (e.g., in CCP discharges during the sheath collapsing phases), which indicates that the electrons are cooling at that moment and location. From equations (3) and (4), the total electron absorbed power $\boldsymbol{J}_e \cdot \boldsymbol{E} = P_e$ is contributed by different power absorption components. A negative net value of a power absorption component indicates that the electrons lose energy through this mechanism under certain conditions. However, the total power absorption averaged over time and space for the entire RF period and discharge region is positive (also in our case, as shown later). Therefore, when a 'negative electron power absorption' is mentioned, it does not mean that the electrons do work on the external circuit.

2.3. Particle-in-cell/Monte Carlo collision simulation

Since the inception of its fundamental framework in the 1960s [115, 116], the PIC simulation has been widely applied in almost all the fields of plasma simulation. In PIC simulation, a large number of particles are followed as they move in the simulation domain. The particle distribution and velocity distribution are directly obtained, therefore, the fully kinetic discharge characteristics including nonlocal and non-equilibrium effects are considered. A detailed description on PIC simulation can be found elsewhere [117, 118]. Boswell and Morey [119] introduced the charged particle-neutral particle collisions into the PIC simulation. On this basis, Vahedi and Surendra [120] further developed the model by taking into account the energy-related cross-sectional data. Nanbu [121, 122] subsequently studied most of the basic aspects in PIC simulation associated with Monte Carlo methods. The method of using PIC simulation to describe the particle motion and using Monte Carlo method to describe the short-range collisions between particles is called PIC/MCC simulation. The PIC simulation has few underlying assumptions or approximations and, therefore, it can provide an accurate and detailed picture of the discharge behavior self-consistently. The two-dimensional simulation performed here is based on our ASTRA PIC/MCC code [106, 123] (see supplementary materials in [106] for the description and the code benchmark with Turner *et al* [124]). As shown in figure 1, a rectangular magnetron with infinite length is adopted and the magnetron discharge can be described in Cartesian coordinate. The plasma is assumed homogeneous in the 'azimuthal' direction and thus the magnetron can be treated in two dimensions. Instability and rotating spokes in the $\boldsymbol{E} \times \boldsymbol{B}$ direction, which have been observed in RFMS [125] discharges, may cause the abnormal transport of electrons and ions [126, 127]. However, the frequency of these oscillations is about hundreds of kHz [125], which is two orders of magnitude lower than the RF. The assumption that the plasma is uniform in the azimuthal direction should not affect the general discussion of electron dynamics on the RF time scale.

3. Results

3.1. Fundamental plasma parameters

In a typical magnetron sputtering discharge, the bulk plasma is highly nonuniform and concentrated above the target surface, where the magnetic field lines are parallel to the target surface and the plasma density is the highest. The target surface in contact with the bulk plasma is often called the 'racetrack' area because this area is subjected to the strongest ion bombardment in conventional DCMS, creating a racetrack groove on the target surface. This racetrack area is also the effective target area for collecting current in DCMS, which is generally about one order of magnitude smaller than the total area of the target surface [128, 129]. For RFMS discharges, once the discharge reaches a periodic steady state, the density and profile of the bulk plasma are basically stable, with small changes in one RF period. To investigate the electron dynamics in detail, figure 2
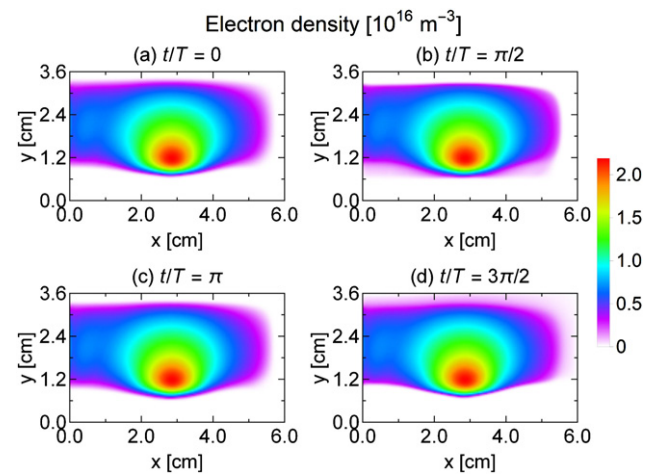

Figure 2. Electron density at different times during an RF period.

shows the spatial distributions of electron density at four typical times during the RF period. The well-confined plasma, with a maximum electron density of about 2.2×10^{16} cm, appears above the target surface at around $x = 2.9$ cm. From figure 2(b), the electrons can only reach the target surface near the phase of $t/T = \pi/2$. At this time, the sinusoidal voltage reaches its positive maximum value; the powered electrode temporarily works as an anode and attracts the electrons. However, the electrons near the target are magnetized, their motion is restricted by the transverse magnetic field lines. For the target area right below the bulk plasma region, the magnetic field is basically parallel to the target surface, which greatly reduces the local electron flux. Therefore, most of the electrons reach the target surface at around $x < 1.5$ and $x > 4$ cm, where the magnetic field lines cross the target surface. This is consistent with previous simulation results [64]. At $t/T = \pi$ the electrons are no longer in contact with the target surface and are blown away at $t/T = 3\pi/2$, when the voltage reaches its negative maximum value and works as a cathode. For a conductive target, this nonuniform electron flux to the target surface does not have much effect on the ion dynamics, because the ions are not magnetized due to their inertia and only response to the time-averaged electric field. However, for an insulating target studied here, the nonuniform electron flux reaching the target surface results in a nonuniform charge accumulation, which distorts the electric potential.

Figure 3 shows the electric potential at different times during the RF period. Since the powered electrode is insulated from the plasma by the dielectric target, the DC bias caused by the magnetic asymmetric effect [36–38, 130] appears on the target surface instead of the electrode. The voltage on the electrode strictly follows a sinusoidal waveform.

The charge accumulation on the dielectric target surface is expected but is not uniform, due to the above-mentioned nonuniform electron flux. As shown in figure 4(a), two negative charge accumulation regions, i.e., $x < 2$ cm and $x > 3.5$ cm, are separated by a positive charge accumulation region along the dielectric target surface. Positive argon ions are accumulated below the bulk plasma region, where the electrons are locally confined by the transverse magnetic
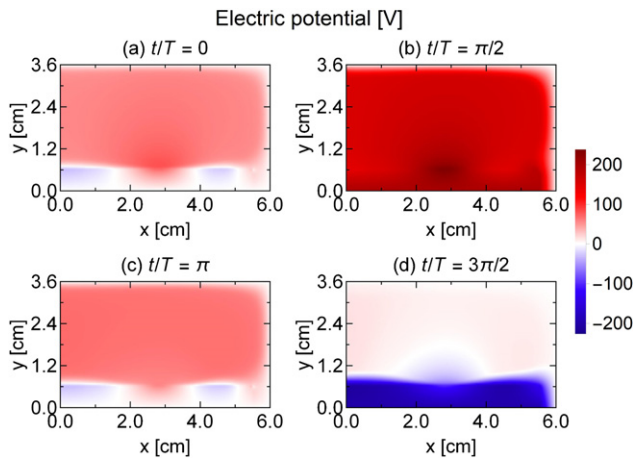
Figure 3. Electric potential at different times during an RF period. Note that the region of $0 \text{ cm} \leqslant x \leqslant 5.5 \text{ cm}$ and $0 \text{ cm} \leqslant y \leqslant 0.6 \text{ cm}$ is occupied by the dielectric target. Perturbed electric potential distribution can be observed along the dielectric target surface at $y = 0.6 \text{ cm}$.

Figure 4. (a) Time-averaged charge density and electric potential, and (b) the IEDF along the dielectric target surface at $0 \text{ cm} \leqslant x \leqslant 5.5 \text{ cm}$ and $y = 0.6 \text{ cm}$.

field and cannot reach the target surface. This nonuniform surface charging results in a perturbation of the potential distribution on the dielectric target surface with a similar profile. This in turn significantly affects the ion energy distribution function (IEDF) of the ions reaching the dielectric target surface. As seen from figure 4(b), the IEDF is spatially dependent along the dielectric target surface. The ion energy at which the IEDF peaks at different locations on the dielectric target surface varies, approximately corresponding to the difference in potential from the highest time-averaged potential to each location. The top marginal plot of figure 4(b) shows a spatially dependent ion flux distribution along the dielectric target surface. Two ion flux peaks appear at both sides of the racetrack region (for convenience, we still refer to the location of the target surface facing the highest plasma density as the racetrack region, although this is not necessarily where the dielectric target surface is most deeply etched, as will be discussed later). From figure 4(b), although the maximum plasma density appears near the racetrack region, the ion energy is less than 20 eV. On the other hand, the ion energy gradually increases beyond the racetrack region, resulting in a relatively uniform energy distribution for all the ions bombarding the dielectric target surface, as shown in the right marginal plot. The distortion of the electric potential distribution caused by the nonuniform charge accumulation has an impact on the electron dynamics, which can be clearly observed from the electric field distribution.

Figure 5 demonstrates the electric field at different times during the RF period. As shown in figures 5(b) and (d), when the electrode voltage is not zero, there is an observable electric field even in the bulk plasma. This is an obvious difference from an unmagnetized RF plasma, in which the electric potential of the bulk plasma is almost constant during an RF period, and the electric field is close to zero [114]. This electric potential drop in the bulk plasma region originates from the confinement of electrons by the magnetic field, which has been observed in DCMS discharges decades ago [131–134]. In
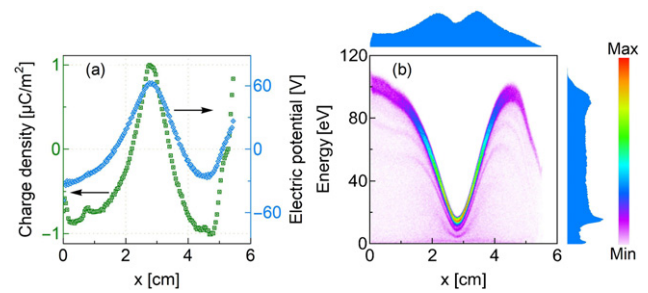
DCMS discharges, the electric potential is funnel-shaped, similar to figure 3(d), but generally with a stronger gradient. This potential profile results in an electric field which accelerates ions toward the target surface and forms a racetrack via sputtering. In RF discharges, ions response to a time-averaged electric field, which generally points from the bulk plasma region to the electrodes. Therefore, for RFMS discharges using a metallic target, the racetrack formed by sputtering is located on the target surface closest to the bulk plasma region. However, for RFMS discharges with a dielectric target, the positive accumulation region on the target surface reduces the local electric field around $x = 2.9 \text{ cm}$, where is the racetrack region in DCMS or RFMS with a metallic target. To sustain the same ion and electron fluxes at all positions on the dielectric target surface within one RF period, two electric field peaks appear at the negative charge accumulation regions. The plasma density is reduced in the locations away from the racetrack region. However, due to the inducement of two electric field peaks, the ions tend to move toward these locations and cause higher ion fluxes, as shown in the top marginal plot of figure 4(b). In addition, the ion energy at these locations is also higher than that in the racetrack region. The high ion fluxes and energies at both sides of the racetrack enhance the local sputtering rate; deeper etching is expected on both sides of the location facing the highest plasma density. This may result in an abnormal erosion profile, that the intensively etched region on a metallic target can be the least eroded on a dielectric target, which has been predicted via numerical calculation and observed in experiments [135].

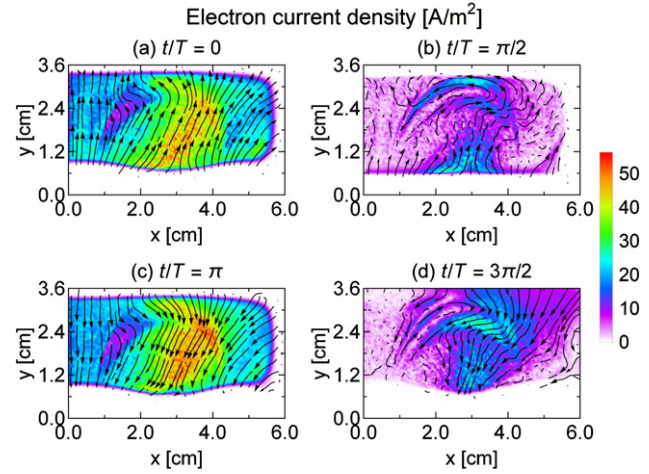### 3.2. Electron current densities

Figure 6 shows the electron current density at different times during an RF period. Note that the direction of electron current is opposite to electron flux since electrons are negatively charged. As shown in figures 6(a) and (b), during the first half of the RF period, the electron current flows mainly from the target to the upper grounded wall, which means that the electrons are attracted by the positive voltage of the electrode and flow to the target surface. From figure 5, the electric field in the negative charge accumulation regions always points to the target surface, even at $t/T = \pi/2$ when the electrode voltage reaches its positive maximum value. However, as shown in figure 6(b), when the electrons leave the bulk plasma region and are close
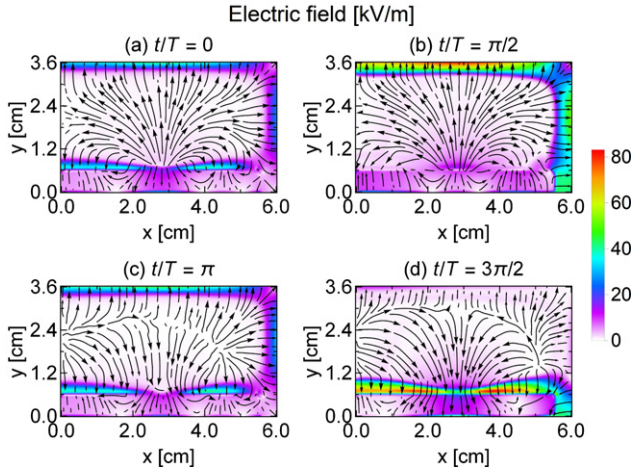
Electric field [kV/m]

Figure 5. Electric field at different times during an RF period. Note that the region of 0 cm $\leqslant x \leqslant$ 5.5 cm and 0 cm $\leqslant y \leqslant$ 0.6 cm is occupied by the dielectric target. Two electric field peaks can be observed on both sides of the racetrack region along the dielectric target surface at $y = 0.6$ cm.

Electron current density [A/m²]

Figure 6. Electron current density in the $x - y$ plane at different times during an RF period.

to the dielectric target surface, they may still reach the target surface at this time under an opposite electric field force, since the velocities of the electrons toward the target are not yet reduced to zero and are not repelled immediately. This is the equilibrium state that the system reaches spontaneously, so that all positions on the target surface receive the same positive and negative charges in one RF period. At around $x = 0$ cm, the magnetic field is basically perpendicular to the target surface; the electron current changes sinusoidally at a RF of 13.56 MHz along the direction of magnetic field. In the bulk plasma region, the electron dynamics becomes more complicated under the influence of the magnetic trap. Taking $x = 2.9$ cm as a symmetry axis, where the plasma density is the highest, the magnetic field distribution is not exactly symmetrical; as a result, the electron current direction is slightly inclined to the upper right, which can be clearly observed in figures 6(a) and (c). In the bulk plasma region, the movement of electrons along the $y -$ direction is constrained by the transverse magnetic field; the cross-field transport of electrons is facilitated via collisions with other particles, and through Bohm diffusion induced by collective effects such as waves and instabilities [136, 137]. From figures 6(b) and (d), before the direction of the electron current changes, the amplitude of the electron current density along the $y -$ direction, J_{ey}, is greatly reduced; the electrons at a distance of 1.5–3 cm from the target surface, where the curvature of the magnetic field is relatively large, can primarily move in the $x -$ direction. However, this phenomenon only occurs when the direction of the electron current changes. During most of an RF period, the electron current density along the $x -$ direction, J_{ex}, is about one order of magnitude lower than J_{ey}, as revealed by previous numerical investigations [62]. As a result, the contribution of the electron current in the $x -$ direction to the electron power absorption is small or even negligible [40], which will be discussed in section 3.3.

The azimuthal electron current density along the $\boldsymbol{E} \times \boldsymbol{B}$ direction, J_{ez}, is shown in figure 7. Note that the unit of J_{ez}

is in kA m^{-2}. Since the electrons are negatively charged, the azimuthal drift direction of electrons is opposite to the direction of J_{ez}, but the same as the $\boldsymbol{E} \times \boldsymbol{B}$ direction. During one RF period, J_{ez} changes sinusoidally at the RF of 13.56 MHz, with a phase difference to J_{ey}. The phase difference and amplitude ratio between J_{ez} and J_{ey} are primarily determined by the electron collision frequency, the electron cyclotron frequency, and the frequency of the RF source. The derivation is briefly described as follows.

We examine a typical location of $x = 2.9$ cm and $y = 1$ cm, where the azimuthal electron current density reaches its peak value. The phase difference and amplitude ratio between J_{ez} and J_{ey} at the selected location are about 0.28π and 26, respectively. To illustrate the relationship between the phase and the amplitude of the electron current density in different directions, in the momentum conservation equation for electrons, equation (2), neglecting the inertial term $m_e (\boldsymbol{\Gamma}_e \cdot \nabla) \boldsymbol{u}_e$ and the pressure term $-\nabla \cdot \overset{\leftrightarrow}{\boldsymbol{\Pi}}_e$, using the approximated form of collision term $(\partial \rho_e / \partial t)_c = -m_e \nu_m n_e \boldsymbol{u}_e$, where ν_m is the electron momentum transfer collision frequency, equation (2) gives

$$m_e n_e \frac{\partial \boldsymbol{u}_e}{\partial t} = -e n_e (\boldsymbol{E} + \boldsymbol{u}_e \times \boldsymbol{B}) - m_e \nu_m n_e \boldsymbol{u}_e. \quad (6)$$

Assuming $\boldsymbol{E}$ and $\boldsymbol{u}_e$ to be of the form $\exp(-i\omega_{RF} t)$, where $i = \sqrt{-1}$ is the imaginary argument, from equation (6), we have

$$\boldsymbol{u}_e \times \boldsymbol{B} = -\boldsymbol{E} - (\nu_m - i\omega_{RF}) m_e \boldsymbol{u}_e / e. \quad (7)$$

Equation (7) can be further simplified as a tensor equation,

$$\epsilon_0 \omega_{pe}^2 \boldsymbol{E} = \overset{\leftrightarrow}{\boldsymbol{A}} \boldsymbol{J}_e, \quad (8)$$

where ϵ_0 is the vacuum permittivity and $\omega_{pe} = \left(e^2 n_e / \epsilon_0 m_e \right)^{1/2}$ the electron plasma frequency. The tensor $\overset{\leftrightarrow}{\boldsymbol{A}}$ is

$$\overset{\leftrightarrow}{\boldsymbol{A}} = \begin{bmatrix} \xi & \Omega_z & -\Omega_y \\ -\Omega_z & \xi & \Omega_x \\ \Omega_y & -\Omega_x & \xi \end{bmatrix}, \quad (9)$$

Electron current density [kA/m²]
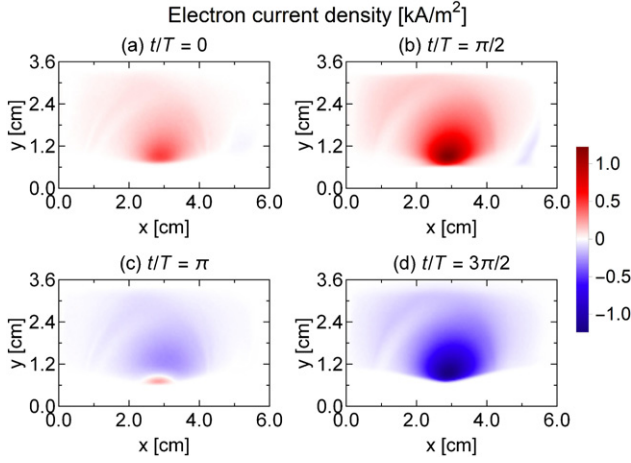
Figure 7. Azimuthal electron current density J_{ez} at different times during an RF period.

where $\xi = \nu_m - i\omega_{RF}$ is a complex frequency, with a real part from the collision between electrons and neutrals, and an imaginary part from the angular frequency of the RF power supply, $\Omega_x = eB_x/m_e$, $\Omega_y = eB_y/m_e$, and $\Omega_z = eB_z/m_e$ are the electron cyclotron frequencies along different directions. At the selected location of $x = 2.9$ cm and $y = 1$ cm, the magnetic field along the $y -$ direction can be ignored. In addition, for a two-dimensional model, $B_z = E_z = 0$ is assumed. Using the above simplification, the relationship between the electron current density in the $y-$ and $z -$ directions can be obtained from equation (8) as

$$J_{ez} = \frac{\Omega_x}{\xi} J_{ey}. \qquad (10)$$

In the selected location, the magnetic field is in the $x -$ direction, the electric field is in the $y -$ direction, and the $\boldsymbol{E} \times \boldsymbol{B}$ drift is in the $z -$ direction. Therefore, the Hall-to-discharge current density ratio in a steady-state direct current magnetized discharge (e.g., DCMS discharge) can be represented as the classical Hall parameter $\frac{J_{ez}}{J_{ey}} = \frac{en_e E_y / B_x}{\sigma_y E_y} = \Omega_x / \nu_m$ [138, 139], where $\sigma_y = \sigma_0(\nu_m^2/\Omega_x^2)$ is the plasma conductivity in the strong magnetic field approximation and $\sigma_0 = \frac{e^2 n_e}{m_e \nu_m}$ is the conductivity in the absence of the magnetic field. Note that when $\omega_{RF} = 0$, equation (10) degenerates to this Hall parameter. However, it has been found that the use of the electron momentum transfer collision frequency ν_m substantially underestimates the cross-field conduction of electrons, usually by orders of magnitude [138]. In addition, as mentioned above, the cross-field diffusion of electrons in magnetron discharges is generally considered to be Bohm diffusion, i.e., diffusion scales as $1/B$ rather than $1/B^2$. In Bohm diffusion, the Hall parameter is usually written in the form of $\omega_e \tau_{eff}$ [140, 141], where ω_e is the cyclotron angular frequency and τ_{eff} the effective momentum transfer time of electrons that includes collective collision processes. Bohm [136] developed a semiempirical conductivity of $\sigma_B = \frac{1}{\omega_e \tau_{eff}} \frac{en_e}{B}$, where $\omega_e \tau_{eff} = 16$ is in close agreement with experimental results, usually within a factor of 3. Substituting the calculated frequencies into equation (10), the phase difference and amplitude ratio between J_{ez} and J_{ey} at the selected

location is 0.298π and 27.4, close to the above observations of 0.28π and 26. The relationship between the electric field and the electron current density can be obtained as well. Substituting equation (10) into the $y -$ direction of equation (8), we have

$$\epsilon_0 \omega_p^2 E_y = \left(\xi + \frac{\Omega_x^2}{\xi} \right) J_{ey}, \qquad (11)$$

the phase difference between E_y and J_{ey} calculated from equation (11) is about 0.3π, consistent with the observation in figures 5 and 6. For unmagnetized plasmas $\Omega_x = 0$, equation (11) gives $J_{ey} = \sigma_p E_y$, where $\sigma_p = \epsilon_0 \omega_{pe}^2/(\nu_m - i\omega_{RF})$ is the plasma conductivity. One can note that the phase differences between the azimuthal current density and the axial current density (i.e., J_{ez} and J_{ey}) and the axial electric field and axial current density (i.e., E_y and J_{ey}) are near identical in absolute value of around 0.3π. Comparing the complex frequencies in equations (10) and (11), we deduce the phase difference of $\frac{\Omega_x}{\xi}/(\xi + \frac{\Omega_x^2}{\xi})$ being $\frac{2\nu_m \omega_{RF}}{\nu_m^2 - \omega_{RF}^2 + \Omega_x^2}$. In a typical RFMS discharge, such as the case studied here, the electron cyclotron frequency Ω_x at a magnetic field of several 100 Gauss is on the order of 10^9 to 10^{10}, while the electron collision frequency ν_m and the RF source frequency ω_{RF} are on the order of 10^7 to 10^8, i.e., about two orders of magnitude smaller. This results in a phase difference between these two complex frequencies of the order of 0.01. Therefore, it can be expected that these two frequencies in equations (10) and (11) should have approximately the same complex phase. The azimuthal current induces a significant Ohmic power absorption, which is the primary electron power absorption component and will be discussed in section 3.3.

Note that the electron current densities presented in figures 6 and 7 are directly obtained from a fully kinetic PIC/MCC simulation without omissions or assumptions, while equations (6)–(11) are derived by neglecting some relatively unimportant terms in the momentum conservation equation (2) in order to study some fundamental relationships in a typical RFMS discharge. The simplifications and discussions in this section do not affect the reliability of the PIC simulation.

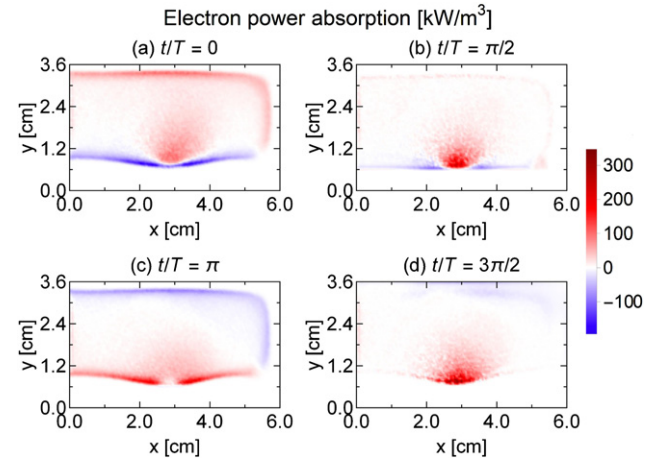### 3.3. Electron power absorption

In RFMS discharges, an RF electric field is applied through an RF power supply, thereby coupling energy to electrons, inducing ionization, and maintaining a stable discharge. Since electrons are responsible for generating ions through ionization collisions, which bombard the target surface to cause sputtering and particle flux for deposition, one of the most fundamental questions in RFMS discharges is how electrons gain and lose energy. Kondo and Nanbu [64] suggested that the $\boldsymbol{E} \times \boldsymbol{B}$ drift and the energy gain via collision with an oscillating sheath are the primary electron power absorption mechanism. Minea and Bretagne [40] provided a simple model for power deposition in RFMS discharges, i.e., by neglecting the inertial and pressure terms in the momentum conservation equation of electrons, the electron power absorption can be shared into the electric field direction and the $\boldsymbol{E} \times \boldsymbol{B}$ direction. Albeit the above studies are based on certain assumptions and are not

complete, they all capture the main characteristics of the electron power absorption in RFMS discharges. Here we demonstrate a self-consistent and complete description of electron power absorption via PIC/MCC simulations and a moment analysis of the Boltzmann equation.

By multiplying figure 5 and 6, we can get the electron power density, $P_e = J_e \cdot E$. Figure 8 shows the electron power density P_e at different times during the RF period. The electron power density is primarily comprised of two components, i.e., an electron power absorption region in the bulk plasma region, which is always positive, and an electron power absorption region that changes sinusoidally with time in the sheath region. At $t/T = 0$, from figure 6(a), the electrons in the bulk plasma region are accelerated by the electric field and moving to the target, resulting in a positive P_e; however, as they approaching the target surface, an opposite electric field appears in the negative charge accumulation region, as shown in figure 5(a), repels the electrons and results in a local negative P_e in figure 8(a). At $t/T = \pi$, from figure 6(c), the electrons near the target surface and in the bulk plasma region are repelled and moving away from the target under the corresponding electric field as shown in figure 5(c); therefore, P_e is positive in both the bulk plasma region and in the sheath. For the same reason, an opposite trend of P_e can be observed near the grounded wall. The most significant electron power absorption occurs at $t/T = \pi/2$ and $t/T = 3\pi/2$; although the electron current densities in the bulk plasma region in figures 6(b) and (d) are reduced, the considerable electric fields observed in figures 5(b) and (d), corresponding to the maximum and minimum voltage values, ensure a significant power absorption in the bulk plasma region. For the electron power absorption near the target, P_e is reduced due to the weakened electric field at $t/T = \pi/2$ and the low electron density near the target at $t/T = 3\pi/2$, respectively. The always positive P_e in the bulk plasma region is a typical feature of the Ohmic power absorption, while the time-modulated P_e in the sheath region is a typical feature of the pressure-induced power absorption [88, 94, 106, 114, 142]. In section 2.2, a consistent and complete description of the electron power absorption is provided by analyzing the moment of the Boltzmann equation for two-dimensional magnetized plasmas. We use this method to decouple the electron power absorption into different components and study them separately, as described below.
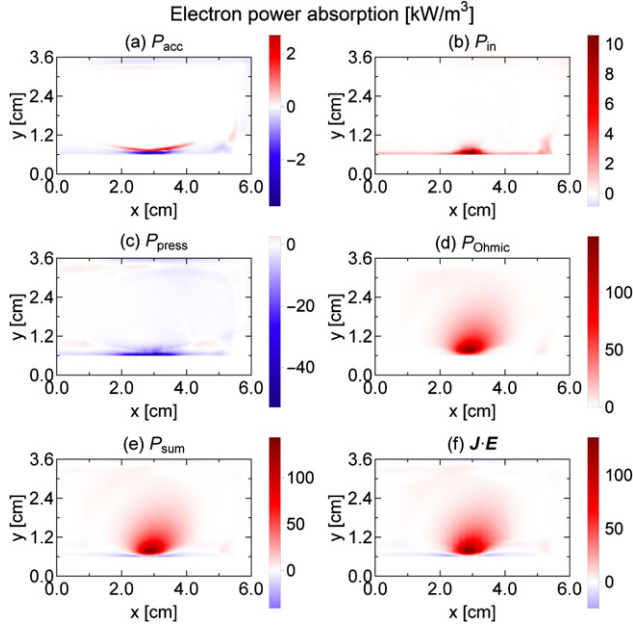
The time-averaged electron power absorption components are calculated from equations (4) and (5) and the results are illustrated in figure 9. The first and second terms on the right-hand side of equation (4), P_{acc} and P_{in}, are the electron power absorption due to electron inertial effects, which are generally assigned to a collisionless phenomenon. The electron drift velocity u_e only has a relatively strong temporal and spatial variation in the sheath region, therefore, the contribution of the inertial components is negligible in the bulk plasma region, but can be observed in the sheath region. As shown in figure 9(a), the acceleration term P_{acc} is positive near the bulk plasma region and negative near the target surface, in the range of about -3.5–2.5 kW m^{-3}. The power absorption induced by the time-modulated electron drift velocity is expected to change sinusoidally with time; however, since the electrons

Electron power absorption [kW/m³]

Figure 8. Electron power density at different times during an RF period.

are attracted and repelled by the target surface within one RF period, the positive and negative power absorption peaks do not overlap in the spatial distribution. The spatiotemporal dynamics of P_{acc} will be shown later. From figure 9(b), the inertial term P_{in} is mostly positive near the target surface, up to 10 kW m^{-3}. The positive power absorption of P_{in} is primarily contributed from the first half of the RF period, which will be discussed later. With the exception of a few cases such as low pressure unmagnetized RF plasmas [88], the contribution of electron inertial effects to electron power absorption is small and generally negligible, but not strictly zero. The contribution of inertial effects to power absorption under various discharge conditions and whether they can be the dominant mechanism under certain conditions might be an interesting topic that deserves further investigation and discussion in the future.

The pressure-induced power absorption P_{press}, as shown in figure 9(c), is negligible in the bulk plasma region and mostly negative near the target surface. As the dominant power absorption mechanism in low pressure RF discharges [88, 94], P_{press} is also a collisionless mechanism and is related to the concept of 'pressure heating' developed by Turner *et al* [73, 75, 79, 96]. However, for magnetized low-pressure RF discharges [96, 106] or RF discharges under very low pressures [143], the dominant mechanism could be the 'Ohmic heating', and the pressure-induced power absorption may even be negative. The last term in equation (4), P_{Ohmic}, is the Ohmic power absorption due to collisions. From figure 9(d), P_{Ohmic} is the dominant mechanism for RFMS discharge under typical conditions investigated here. This result is similar to the previous one-dimensional PIC/MCC simulation investigation on magnetized RF discharges [106]. Most of the Ohmic power absorption appears in the bulk plasma region, where the azimuthal electron current plays the most important role and the Ohmic power absorption is mostly contributed from the azimuthal direction, since the Ohmic power absorption is proportional to the square of the electron current density in the corresponding direction. The contribution of Ohmic power absorption in the $x-$, $y-$, and $z-$directions is 0.6%, 2.1%, and 97.3%, respectively.

Figure 9. Spatial distributions of time-averaged electron power absorption components: (a) power absorption due to the acceleration term, P_{acc}; (b) power absorption due to the inertial term, P_{in}; (c) power absorption due to pressure-induced effects, P_{press}; (d) power absorption due to collisional dynamics, P_{Ohmic}; (e) the sum of the above four power absorption components, P_{sum}; (f) electron power density calculated from $\boldsymbol{J}_{\mathrm{e}} \cdot \boldsymbol{E}$.

Figure 9(e) shows the sum of the above-mentioned power absorption components, $P_{\mathrm{sum}} = P_{\mathrm{acc}} + P_{\mathrm{in}} + P_{\mathrm{press}} + P_{\mathrm{Ohmic}}$. Comparing with figure 9(f), the power absorption P_{sum} from the sum of each component matches well with the power absorption directly calculated from $\boldsymbol{J}_{\mathrm{e}} \cdot \boldsymbol{E}$. The contribution from inertial terms can be neglected and the power absorption can approximately be decoupled as the positive Ohmic power absorption in the bulk plasma region in figure 9(d), and the negative pressure-induced power absorption near the target surface in figure 9(c). However, the time-averaged electron power absorption cannot provide the temporal dynamic information; in this respect, the spatiotemporal distribution of power absorption is required.

The temporal dynamics of the electron power absorption at $x = 3$ cm is shown in figure 10. From figures 10(a) and (c), the amplitude of P_{acc} in one RF period is up to 190 kW m^{-3}, approximately equivalent to the amplitude of P_{press}. The power absorption from the inertial term, P_{in}, as shown in figure 10(b), is primarily contributed from the first half of the RF period, when the electrons are attracted to the target surface. The pressure-induced power absorption P_{press} in figure 10(c) shows a typical spatiotemporal distribution for low pressure RF plasmas. For the Ohmic power absorption, as shown in figure 10(d), two maximum values appear around $t/T = \pi/2$ and $t/T = 3\pi/2$, where the azimuthal electron current achieves its maximum. Comparing figure 10(e) with figure 10(f), the spatiotemporal power absorption P_{sum} from the sum of each component is in good agreement with $\boldsymbol{J}_{\mathrm{e}} \cdot \boldsymbol{E}$ as well. The spatiotemporal power absorption near the top wall at $y = 3$–3.6 cm, where the magnetic field is relatively
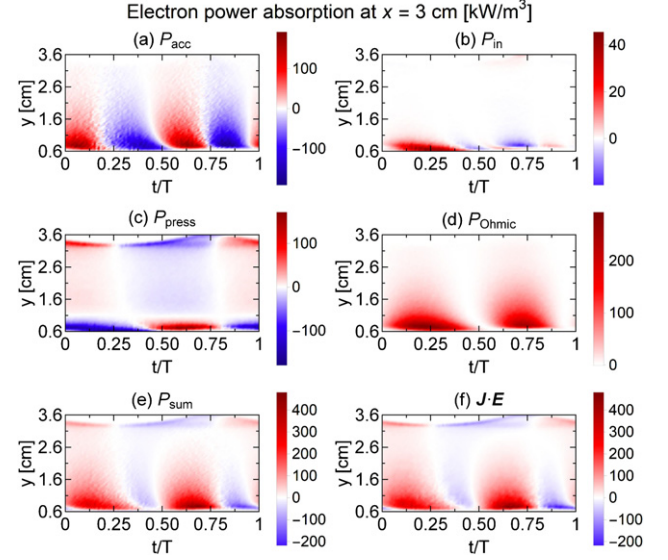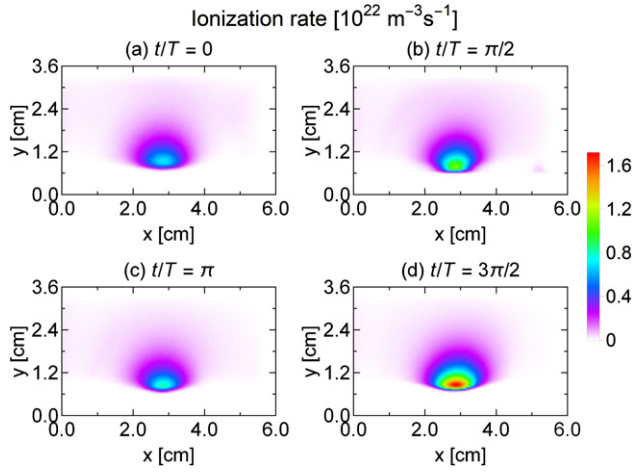

Figure 10. Temporal dynamics of electron power absorption components at $x = 3$ cm: (a) P_{acc}; (b) P_{in}; (c) P_{press}; (d) P_{Ohmic}; (e) P_{sum}; (f) $\boldsymbol{J}_{\mathrm{e}} \cdot \boldsymbol{E}$.

weak (less than 20 G), is primarily contributed by P_{press}; other components can barely be observed, similar to the unmagnetized case. Due to the strong negative P_{press} near the target surface during the first half of the RF period, the maximum power absorption $\boldsymbol{J}_{\mathrm{e}} \cdot \boldsymbol{E}$ appears during the second half of the RF period. The negative $\boldsymbol{J}_{\mathrm{e}} \cdot \boldsymbol{E}$ in the bulk plasma region at around $t/T = 0.4$ and $t/T = 0.9$ is contributed from P_{acc}. Comparing this RFMS discharge with a typical low-pressure unmagnetized RF discharge [71], the amplitude of the power absorption induced by inertial effects is significantly increased, which is equivalent to the pressure-induced power absorption; however, the time-averaged contribution is still negligible. Revisiting the study on electron power absorption in RFMS discharges by Minea *et al* [40], their assumptions and conclusions are still correct under the conditions investigated here; by neglecting the inertial and pressure terms, which are not dominant in the bulk plasma region, $\boldsymbol{J}_{\mathrm{e}} \cdot \boldsymbol{E}$ can be decomposed into the power absorption in the electric field direction and in the $\boldsymbol{E} \times \boldsymbol{B}$ direction. According to their analytical model, the ratio of $P_{\mathrm{Ohmic}z}/P_{\mathrm{Ohmic}y}$ can be derived from the electron momentum transfer collision frequency ν_{m}, the electron cyclotron angular frequency Ω_x, and the RF source frequency ω_{RF}. At the location of $x = 2.9$ cm and $y = 1$ cm, $\omega_{\mathrm{RF}}/\Omega_x \approx 0.03$ and $\nu_{\mathrm{m}}/\Omega_x \approx 0.02$, the Ohmic power absorption ratio between the $z-$ and $y-$directions derived by the analytical model [40] is about $P_{\mathrm{Ohmic}z}/P_{\mathrm{Ohmic}y} \approx 50$, comparable to the contribution of Ohmic power absorption in the $y-$ and $z-$directions directly calculated from the PIC simulation, i.e., 2.1% and 97.3%.

3.4. Ionization dynamics

The power absorbed by electrons in the bulk plasma region is dissipated through inelastic collisions, i.e., ionization and excitation for the RFMS discharge simulated here. Figure 11 shows the ionization rate at different times during the RF
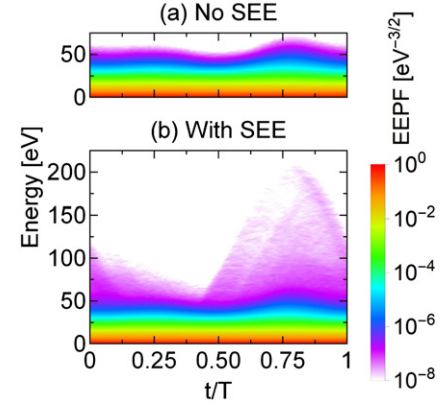
Figure 11. Ionization rate at different times during an RF period.

Figure 12. Temporal EEPF collected in the entire simulation region (a) without and (b) with secondary electrons.

period, the excitation rate has similar profiles. From the ionization rate profile at different times, ionization occurs mainly in the bulk plasma region, where is therefore often referred to as the 'ionization region' [41]. At $t/T = 3\pi/2$, as shown in figure 11(d), the ionization rate reaches its maximum of up to 1.7×10^{22} (m^3 s), when the electrons are repelled from the target and accelerated along the magnetic field lines to the bulk plasma region. Comparing figures 11 and 8, the power absorption and dissipation of electrons in the bulk plasma region are approximately synchronized in time and space, which is expected in magnetized plasmas. Previous investigations have shown that a magnetic field applied perpendicular to the electric field results in an electron trapping [137], and collisional bulk electron power absorption becomes dominant [144]. This is because the magnetic field weakens the electron diffusion in the configuration space but enhances the diffusion in the energy space [145].

Secondary electron emission (SEE) induced by positive ions is of essential importance in sustaining the DC magnetron discharges [141, 146]. However, for RF plasmas, especially when the discharge is operated in low-pressure α mode, secondary electrons are not necessary and their contribution is negligible. To illustrate the influence of SEE in the RFMS discharge investigated here, an energy-dependent SEE coefficient for argon ions is adopted as [147, 148]:

$$\gamma_i(\varepsilon) = \frac{0.006\varepsilon}{1 + (\varepsilon/10)} + \frac{1.05 \times 10^{-4}(\varepsilon - 80)^{1.2}}{(1 + \varepsilon/8000)^{1.5}}, \quad (12)$$

where ε is the argon ion energy. Although this coefficient was originally developed for dirty surfaces, such as oxidized metal surfaces, here we adopt it as an approximation to theoretically investigate the influence of an energy-dependent SEE coefficient in RFMS discharges. With SEE, the RFMS discharge is simulated under the same conditions. Comparing the results with SEE and the above-mentioned results without SEE, there is no observable difference except for the electron energy possibility function (EEPF). The results that include the effect of SEE are not shown here because the influence is small and little difference is observed as compared with the results without including SEE. For example, the increase in electron density

is less than 0.6% by considering the SEE. The charging effect of the dielectric surface and the perturbed potential profile is not significantly modified by the inclusion of SEE in the simulation as well. Note that combining the energy-dependent SEE coefficient of equation (12) and the spatially dependent IEDF shown in figure 4(b), it can be expected that the EEPF is also spatially dependent in the $x-$ direction, albeit this has limited effect on typical RFMS discharges.

Note that the SEE coefficient used in the PIC simulation is not the apparent SEE [149] commonly used in fluid simulations. The SEE processes can be treated with either an apparent or a true SEE coefficient in numerical simulations [150]. In PIC simulations, the true SEE treatment is used and a predetermined SEE coefficient is adopted to emit secondary electrons at the location where the ion bombards the surface. When the SEE coefficient is less than one, the coefficient is used as the probability to determine whether the secondary electrons are emitted; when the SEE coefficient is greater than one, secondary electrons with a quantity of the integer part of the coefficient are emitted, and the fractional part of the coefficient is used as the probability to determine whether secondary electrons are emitted. This is an approach with first-principle nature, and no prior assumptions are made about the location of SEE.

Figure 12 shows the temporal EEPF collected in the entire simulation region without and with secondary electrons. Without SEE, as shown in figure 12(a), the maximum electron energy is around 50 eV, which corresponds to the potential difference between the target surface and the bulk plasma region. With SEE, as shown in figure 12(b), a high energy tail of up to more than 200 eV appears, corresponding to the maximum potential of the RF sheath. This high energy tail comes from the high-energy ballistic electrons (HEBEs) that originate from secondary electrons in low-pressure RF plasmas. However, in a typical low-pressure RFMS discharge, the contribution of secondary electrons to ionization and electron power absorption is negligible, which is consistent with previous studies [62, 64]. This is because the number of ballistic secondary electrons are very small, which was found to be several orders of magnitude less compare to the bulk density. A detailed discussion of HEBEs can be found in [151].

4. Conclusions

The electron dynamics in a typical electropositive RFMS discharge operated in argon at a frequency of 13.56 MHz, a driving voltage of 200 V, and a gas pressure of 10 mTorr is studied via a fully kinetic, 2d3v PIC/MCC electrostatic simulation. The spatiotemporal dynamics of the fundamental parameters, such as electron densities, electric potentials and fields, as well as electron current densities during one RF period is demonstrated in detail. Due to the influence of magnetic trap on the electron transport, a spatially dependent charging is observed on the dielectric target surface, resulting in a reduction in the electric field at the target surface closest to the bulk plasma, and an enhancement on both sides of the field reduction region. This results in a spatially dependent ion energy distribution along the target surface, which in turn may cause an abnormal erosion profile, that the intensively etched region on a metallic target can be the least eroded on a dielectric target. The phase difference and amplitude ratio between electron current densities in different directions are primarily determined by the electron cyclotron angular frequency, the electron momentum transfer collision frequency, and the RF source frequency. The amplitude ratio of the electron current densities in the $\boldsymbol{E} \times \boldsymbol{B}$ and the electric field directions, observed in the bulk plasma region, is about 27.4, in approximate agreement with the classical Hall parameter in Bohm diffusion. The electron power absorption mechanism is investigated using a self-consistent, spatiotemporal resolved moment analysis of the Boltzmann equation, for which the input parameters are taken from PIC/MCC simulations. In contrast to a variety of previous analyses on electron power absorption in RFMS discharges, this method makes no assumptions other than which inherited from PIC simulations, therefore provides a fully self-consistent and complete description of this complicated phenomenon. The dominant electron power absorption mechanism on time- and space-average is the Ohmic power absorption, mostly contributed from the $\boldsymbol{E} \times \boldsymbol{B}$ direction. The power absorption due to electron inertial effects is negligible on time-average; therefore, the electron power absorption can be primarily decoupled into the positive power absorption in the bulk plasma region due to collisional dynamics, and the negative power absorption near the target surface due to pressure-induced effects. The ionization rate reaches its maximum during the second half of the RF period, when the electrons are repelled from the target and accelerated to the bulk plasma region. The power absorption and dissipation of electrons in the bulk plasma region are approximately synchronized in time and space, suggesting a suppression of the nonlocal electron motion in magnetron discharges. The contribution of secondary electrons is negligible under typical RFMS discharge conditions investigated here.

Acknowledgments

Data availability statement

The data that support the findings of this study are available upon reasonable request from the authors.

ORCID iDs

Bocong Zheng https://orcid.org/0000-0002-6052-3693
Yangyang Fu https://orcid.org/0000-0001-9593-3177
Thomas Schuelke https://orcid.org/0000-0001-7531-4600
Qi Hua Fan https://orcid.org/0000-0002-8612-1326

References

[1] Lieberman M A and Lichtenberg A J 2005 *Principles of Plasma Discharges and Materials Processing* (New York: Wiley)
[2] Chabert P and Braithwaite N 2011 *Physics of Radio-Frequency Plasmas* (Cambridge: Cambridge University Press)
[3] Anders A 2017 *J. Appl. Phys.* **121** 171101
[4] Gudmundsson J T 2020 *Plasma Sources Sci. Technol.* **29** 113001
[5] Kim K H, Park K C and Ma D Y 1997 *J. Appl. Phys.* **81** 7764
[6] Kim K-K, Song J-H, Jung H-J, Choi W-K, Park S-J and Song J-H 2000 *J. Appl. Phys.* **87** 3573
[7] Shi W S, Agyeman O and Xu C N 2002 *J. Appl. Phys.* **91** 5640
[8] Jeong S-H, Kim B-S and Lee B-T 2003 *Appl. Phys. Lett.* **82** 2625
[9] Chen L-Y, Chen W-H, Wang J-J, Hong F C-N and Su Y-K 2004 *Appl. Phys. Lett.* **85** 5628
[10] Lin C-C, Chen S-Y, Cheng S-Y and Lee H-Y 2004 *Appl. Phys. Lett.* **84** 5040
[11] Hwang D-K, Kim H-S, Lim J-H, Oh J-Y, Yang J-H, Park S-J, Kim K-K, Look D C and Park Y S 2005 *Appl. Phys. Lett.* **86** 151917
[12] Chang W-Y, Lai Y-C, Wu T-B, Wang S-F, Chen F and Tsai M-J 2008 *Appl. Phys. Lett.* **92** 022110
[13] Sirghi L 2016 *Plasma Sources Sci. Technol.* **25** 033003
[14] Park K-I, Xu S, Liu Y, Hwang G-T, Kang S-J L, Wang Z L and Lee K J 2010 *Nano Lett.* **10** 4939
[15] Fu F, Feurer T, Jäger T, Avancini E, Bissig B, Yoon S, Buecheler S and Tiwari A N 2015 *Nat. Commun.* **6** 8932
[16] Yang C C, Chen M S, Hong T J, Wu C M, Wu J M and Wu T B 1995 *Appl. Phys. Lett.* **66** 2643
[17] Zhou Z H, Xue J M, Li W Z, Wang J, Zhu H and Miao J M 2004 *Appl. Phys. Lett.* **85** 804
[18] Wu J and Wang J 2010 *Acta Mater.* **58** 1688
[19] Kim T W, Lee D U and Yoon Y S 2000 *J. Appl. Phys.* **88** 3759
[20] Li W-J and Fu Z-W 2010 *Appl. Surf. Sci.* **256** 2447
[21] Tsai M S, Sun S C and Tseng T Y 1997 *J. Appl. Phys.* **82** 3482
[22] Lai C-H, Lin S-J, Yeh J-W and Chang S-Y 2006 *Surf. Coat. Technol.* **201** 3275
[23] Nelea V, Morosanu C, Iliescu M and Mihailescu I N 2003 *Surf. Coat. Technol.* **173** 315
[24] Nelea V, Morosanu C, Iliescu M and Mihailescu I N 2004 *Appl. Surf. Sci.* **228** 346
[25] Vlakhov E S, Chakalov R A, Chakalova R I, Nenkov K A, Dörr K, Handstein A and Müller K-H 1998 *J. Appl. Phys.* **83** 2152
[26] Anders A 2010 *Thin Solid Films* **518** 4087

[27] Tsuda O, Tatebayashi Y, Takamura Y Y and Yoshida T 1999 *Plasma Sources Sci. Technol.* **8** 392

[28] Gahan D, Daniels S, Hayden C, Scullin P, O'Sullivan D, Pei T and Hopkins M B 2012 *Plasma Sources Sci. Technol.* **21** 024004

[29] Bornholdt S, Ye J, Ulrich S and Kersten H 2012 *J. Appl. Phys.* **112** 123301

[30] Bornholdt S, Itagaki N, Kuwahara K, Wulff H, Shiratani M and Kersten H 2013 *Plasma Sources Sci. Technol.* **22** 025019

[31] Ries S, Banko L, Hans M, Primetzhofer D, Schneider J M, Ludwig A, Awakowicz P and Schulze J 2019 *Plasma Sources Sci. Technol.* **28** 114001

[32] Lin I 1985 *J. Appl. Phys.* **58** 2981

[33] Ohtsu Y, Matsuo H and Fujita H 1996 *Plasma Sources Sci. Technol.* **5** 344

[34] Li Y, Iizuka S and Sato N 1996 *Plasma Sources Sci. Technol.* **5** 241

[35] Huang F, Ye C, He H, Liu Y, Wang X and Ning Z 2013 *Plasma Sources Sci. Technol.* **23** 015003

[36] Oberberg M, Kallähn J, Awakowicz P and Schulze J 2018 *Plasma Sources Sci. Technol.* **27** 105018

[37] Oberberg M, Engel D, Berger B, Wölfel C, Eremin D, Lunze J, Brinkmann R P, Awakowicz P and Schulze J 2019 *Plasma Sources Sci. Technol.* **28** 115021

[38] Oberberg M *et al* 2020 *Plasma Sources Sci. Technol.* **29** 075013

[39] Lieberman M A, Lichtenberg A J and Savas S E 1991 *IEEE Trans. Plasma Sci.* **19** 189

[40] Minea T M and Bretagne J 2003 *Plasma Sources Sci. Technol.* **12** 97

[41] Raadu M A, Axnäs I, Gudmundsson J T, Huo C and Brenning N 2011 *Plasma Sources Sci. Technol.* **20** 065007

[42] Huo C, Raadu M A, Lundin D, Gudmundsson J T, Anders A and Brenning N 2012 *Plasma Sources Sci. Technol.* **21** 045004

[43] Huo C, Lundin D, Raadu M A, Anders A, Gudmundsson J T and Brenning N 2013 *Plasma Sources Sci. Technol.* **22** 045005

[44] Huo C, Lundin D, Raadu M A, Anders A, Gudmundsson J T and Brenning N 2014 *Plasma Sources Sci. Technol.* **23** 025017

[45] Zheng B C, Meng D, Che H L and Lei M K 2015 *J. Appl. Phys.* **117** 203302

[46] Brenning N, Gudmundsson J T, Lundin D, Minea T, Raadu M A and Helmersson U 2016 *Plasma Sources Sci. Technol.* **25** 065024

[47] Huo C, Lundin D, Gudmundsson J T, Raadu M A, Bradley J W and Brenning N 2017 *J. Phys. D: Appl. Phys.* **50** 354003

[48] Zheng B C, Wu Z L, Wu B, Li Y G and Lei M K 2017 *J. Appl. Phys.* **121** 171901

[49] Brenning N, Gudmundsson J T, Raadu M A, Petty T J, Minea T and Lundin D 2017 *Plasma Sources Sci. Technol.* **26** 125003

[50] Lundin D, Gudmundsson J T, Brenning N, Raadu M A and Minea T M 2017 *J. Appl. Phys.* **121** 171917

[51] Zheng B *et al* 2019 *IEEE Trans. Plasma Sci.* **47** 193

[52] Cui S *et al* 2019 *J. Appl. Phys.* **125** 063302

[53] Cui S *et al* 2020 *J. Appl. Phys.* **127** 023301

[54] Chen L *et al* 2020 *Plasma Sources Sci. Technol.* **29** 025016

[55] Maaloul L, Morel S and Stafford L 2012 *J. Vac. Sci. Technol.* A **30** 021301

[56] Kushner M J 2003 *J. Appl. Phys.* **94** 1436

[57] Rauf S 2005 *Plasma Sources Sci. Technol.* **14** 329

[58] Yang Y and Kushner M J 2007 *J. Vac. Sci. Technol.* A **25** 1420

[59] Bultinck E and Bogaerts A 2011 *Plasma Sources Sci. Technol.* **20** 045013

[60] Bogaerts A, Bultinck E, Kolev I, Schwaederlé L, Van Aeken K, Buyle G and Depla D 2009 *J. Phys. D: Appl. Phys.* **42** 194018

[61] Minea T M, Bretagne J and Gousset G 1999 *IEEE Trans. Plasma Sci.* **27** 94

[62] Minea T M, Bretagne J, Gousset G, Magne L, Pagnon D and Touzeau M 1999 *Surf. Coat. Technol.* **116-119** 558

[63] Minea T M, Bretagne J, Pagnon D and Touzeau M 2000 *J. Phys. D: Appl. Phys.* **33** 1884

[64] Kondo S and Nanbu K 2001 *J. Vac. Sci. Technol.* A **19** 838

[65] Bretagne J, Laporte C B, Gousset G, Leroy O, Minea T M, Pagnon D, Poucques L d and Touzeau M 2003 *Plasma Sources Sci. Technol.* **12** S33

[66] Yonemura S and Nanbu K 2003 *IEEE Trans. Plasma Sci.* **31** 479

[67] Yonemura S and Nanbu K 2005 *IEEE Trans. Plasma Sci.* **33** 350

[68] Yonemura S and Nanbu K 2006 *Thin Solid Films* **506-507** 517

[69] Benyoucef D and Yousfi M 2013 *IEEE Trans. Plasma Sci.* **41** 829

[70] Benyoucef D and Yousfi M 2014 *Plasma Sources Sci. Technol.* **23** 044007

[71] Wilczek S, Schulze J, Brinkmann R P, Donkó Z, Trieschmann J and Mussenbrock T 2020 *J. Appl. Phys.* **127** 181101

[72] Godyak V A and Piejak R B 1990 *Phys. Rev. Lett.* **65** 996

[73] Turner M M 1995 *Phys. Rev. Lett.* **75** 1312

[74] Lieberman M A and Godyak V A 1998 *IEEE Trans. Plasma Sci.* **26** 955

[75] Gozadinos G, Turner M M and Vender D 2001 *Phys. Rev. Lett.* **87** 135004

[76] You S J, Ahn S K and Chang H Y 2006 *Appl. Phys. Lett.* **89** 171502

[77] Mussenbrock T and Brinkmann R P 2006 *Appl. Phys. Lett.* **88** 151503

[78] Mussenbrock T, Brinkmann R P, Lieberman M A, Lichtenberg A J and Kawamura E 2008 *Phys. Rev. Lett.* **101** 085004

[79] Turner M M 2009 *J. Phys. D: Appl. Phys.* **42** 194008

[80] Liu Y-X, Zhang Q-Z, Jiang W, Hou L-J, Jiang X-Z, Lu W-Q and Wang Y-N 2011 *Phys. Rev. Lett.* **107** 055002

[81] Donkó Z, Schulze J, Czarnetzki U, Derzsi A, Hartmann P, Korolov I and Schüngel E 2012 *Plasma Phys. Control. Fusion* **54** 124003

[82] Lafleur T, Delattre P A, Johnson E V and Booth J P 2012 *Appl. Phys. Lett.* **101** 124104

[83] Lafleur T, Boswell R W and Booth J P 2012 *Appl. Phys. Lett.* **100** 194101

[84] Lafleur T and Boswell R W 2012 *Phys. Plasmas* **19** 023508

[85] Lafleur T, Chabert P, Turner M M and Booth J P 2013 *Phys. Plasmas* **20** 124503

[86] Schulze J, Donkó Z, Derzsi A, Korolov I and Schuengel E 2014 *Plasma Sources Sci. Technol.* **24** 015019

[87] Lafleur T, Chabert P, Turner M M and Booth J P 2014 *Plasma Sources Sci. Technol.* **23** 015016

[88] Lafleur T, Chabert P and Booth J P 2014 *Plasma Sources Sci. Technol.* **23** 035010

[89] Lafleur T and Chabert P 2015 *Plasma Sources Sci. Technol.* **24** 044002

[90] Brinkmann R P 2015 *Plasma Sources Sci. Technol.* **25** 014001

[91] Schulze J and Mussenbrock T 2016 *Plasma Sources Sci. Technol.* **25** 020401

[92] Gudmundsson J T and Snorrason D I 2017 *J. Appl. Phys.* **122** 193302

[93] Gudmundsson J T, Snorrason D I and Hannesdottir H 2018 *Plasma Sources Sci. Technol.* **27** 025009

[94] Schulze J, Donkó Z, Lafleur T, Wilczek S and Brinkmann R P 2018 *Plasma Sources Sci. Technol.* **27** 055010

[95] Rauf S 2020 *Plasma Sources Sci. Technol.* **29** 095019

[96] Turner M M, Hutchinson D A W, Doyle R A and Hopkins M B 1996 *Phys. Rev. Lett.* **76** 2069

[97] Park J-C and Kang B 1997 *IEEE Trans. Plasma Sci.* **25** 499

[98] You S J, Chung C W, Bai K H and Chang H Y 2002 *Appl. Phys. Lett.* **81** 2529

[99] Lee S H, You S J, Chang H Y and Lee J K 2007 *J. Vac. Sci. Technol.* A **25** 455

[100] You S J, Park G Y, Kwon J H, Kim J H, Chang H Y, Lee J K, Seong D J and Shin Y H 2010 *Appl. Phys. Lett.* **96** 101504

[101] You S J *et al* 2011 *Thin Solid Films* **519** 6981

[102] Ohtsu Y and Yanagise T 2015 *Plasma Sources Sci. Technol.* **24** 034005

[103] Dujko S, Bošnjaković D, White R D and Lj Petrović Z 2015 *Plasma Sources Sci. Technol.* **24** 054006

[104] Yang S, Innocenti M E, Zhang Y, Yi L and Jiang W 2017 *J. Vac. Sci. Technol.* A **35** 061311

[105] Binwal S, Joshi J K, Karkari S K, Kaw P K and Nair L 2018 *Phys. Plasmas* **25** 033506

[106] Zheng B, Wang K, Grotjohn T, Schuelke T and Fan Q H 2019 *Plasma Sources Sci. Technol.* **28** 09LT03

[107] Wang L, Wen D-Q, Hartmann P, Donkó Z, Derzsi A, Wang X-F, Song Y-H, Wang Y-N and Schulze J 2020 *Plasma Sources Sci. Technol.* **29** 105004

[108] Hutchinson D A W, Turner M M, Doyle R A and Hopkins M B 1995 *IEEE Trans. Plasma Sci.* **23** 636

[109] Lieberman M A 1989 *J. Appl. Phys.* **65** 4186

[110] Lieberman M A and Savas S E 1990 *J. Vac. Sci. Technol.* A **8** 1632

[111] Koenig H R and Maissel L I 1970 *IBM J. Res. Dev.* **14** 168

[112] Surendra M and Dalvie M 1993 *Phys. Rev.* E **48** 3914

[113] Proto A and Gudmundsson J T 2020 *J. Appl. Phys.* **128** 113302

[114] Liu Y, Booth J-P and Chabert P 2018 *Plasma Sources Sci. Technol.* **27** 025006

[115] Buneman O 1959 *Phys. Rev.* **115** 503

[116] Dawson J 1962 *Phys. Fluids* **5** 445

[117] Birdsall C K and Langdon A B 1985 *Plasma Physics via Computer Simulation* (New York: McGraw-Hill)

[118] Hockney R W and Eastwood J W 1988 *Computer Simulation Using Particles* (Boca Raton, FL: CRC Press)

[119] Boswell R W and Morey I J 1988 *Appl. Phys. Lett.* **52** 21

[120] Vahedi V and Surendra M 1995 *Comput. Phys. Commun.* **87** 179

[121] Nanbu K, Morimoto T and Suetani M 1999 *IEEE Trans. Plasma Sci.* **27** 1379

[122] Nanbu K 2000 *IEEE Trans. Plasma Sci.* **28** 971

[123] Zheng B, Fu Y, Wen D-q, Wang K, Schuelke T and Hua Fan Q 2020 *J. Phys. D: Appl. Phys.* **53** 435201

[124] Turner M M, Derzsi A, Donkó Z, Eremin D, Kelly S J, Lafleur T and Mussenbrock T 2013 *Phys. Plasmas* **20** 013507

[125] Panjan M 2019 *J. Appl. Phys.* **125** 203303

[126] Panjan M, Franz R and Anders A 2014 *Plasma Sources Sci. Technol.* **23** 025007

[127] Franz R, Clavero C, Kolbeck J and Anders A 2016 *Plasma Sources Sci. Technol.* **25** 015022

[128] Anders A and Oks E 2009 *J. Appl. Phys.* **106** 023306

[129] Anders A 2010 *Surf. Coat. Technol.* **204** 2864

[130] Yang S, Chang L, Zhang Y and Jiang W 2018 *Plasma Sources Sci. Technol.* **27** 035008

[131] Bradley J W, Thompson S and Gonzalvo Y A 2001 *Plasma Sources Sci. Technol.* **10** 490

[132] Mishra A, Kelly P J and Bradley J W 2010 *Plasma Sources Sci. Technol.* **19** 045014

[133] Mishra A, Kelly P J and Bradley J W 2011 *J. Phys. D: Appl. Phys.* **44** 425201

[134] Rauch A, Mendelsberg R J, Sanders J M and Anders A 2012 *J. Appl. Phys.* **111** 083302

[135] Kuroiwa S, Mine T, Yagisawa T and Makabe T 2005 *J. Vac. Sci. Technol.* B **23** 2218

[136] Bohm D 1949 *The Characteristics of Electrical Discharges in Magnetic Fields* ed A Guthrie and R K Wakerling (New York: McGraw-Hill) ch 2 pp 13–76

[137] Chen F 2016 *Introduction to Plasma Physics and Controlled Fusion* (Berlin: Springer)

[138] Rossnagel S M and Kaufman H R 1987 *J. Vac. Sci. Technol.* A **5** 88

[139] Rossnagel S M and Kaufman H R 1987 *J. Vac. Sci. Technol.* A **5** 2276

[140] Brenning N, Merlino R L, Lundin D, Raadu M A and Helmersson U 2009 *Phys. Rev. Lett.* **103** 225003

[141] Gudmundsson J T, Brenning N, Lundin D and Helmersson U 2012 *J. Vac. Sci. Technol.* A **30** 030801

[142] Vass M, Wilczek S, Lafleur T, Brinkmann R P, Donkó Z and Schulze J 2020 *Plasma Sources Sci. Technol.* **29** 025019

[143] Vass M, Wilczek S, Lafleur T, Brinkmann R P, Donkó Z and Schulze J 2020 *Plasma Sources Sci. Technol.* **29** 085014

[144] You S J, Kim S S and Chang H Y 2004 *Appl. Phys. Lett.* **85** 4872

[145] You S J and Chang H Y 2006 *Phys. Plasmas* **13** 043503

[146] Thornton J A 1978 *J. Vac. Sci. Technol.* **15** 171

[147] Phelps A V and Petrovic Z L 1999 *Plasma Sources Sci. Technol.* **8** R21

[148] Daksha M, Derzsi A, Wilczek S, Trieschmann J, Mussenbrock T, Awakowicz P, Donkó Z and Schulze J 2017 *Plasma Sources Sci. Technol.* **26** 085006

[149] Fu Y, Zhang P, Verboncoeur J P and Wang X 2020 *Plasma Res. Express* **2** 013001

[150] Donkó Z 2001 *Phys. Rev.* E **64** 026401

[151] Fu Y, Zheng B, Wen D-Q, Zhang P, Fan Q H and Verboncoeur J P 2020 *Plasma Sources Sci. Technol.* **29** 09LT01